Supporting information

Integrated Thermal Management-Sensing-Actuation Functional Artificial Muscles

Lufeng Wang[1#], Shiju Yang[1#], Lixue Yang[1], Yang Guo[2], Yiyao Zhang[1], Xiong Li[4], Hongzhi Wang[2,3], Liping Zhu[2], Meifang Zhu[2], Jiuke Mu[1]**

*Corresponding author. Email: zhulp@dhu.edu.cn; jiukemu@tju.edu.cn

Table of Contents

1. The fabrication details of FCAM

In this study, we delineate the fabrication process of fluidic cooling artificial muscles (FCAM), a critical innovation designed to augment the thermal regulation and actuation capabilities of biomimetic systems. The fluid pump is crafted by winding multiple Thermoplastic Polyurethane (TPU) fibers around core shafts (metal rods or metal rods coated with silicon) of varying diameters. Between layers of TPU fibers, spiral electrodes are sequentially inserted in a 2:1 ratio. These electrodes are made from copper wires or copper wires wrapped with Carbon Nanotubes (CNTs). Following assembly, the entire structure is subjected to a heat treatment at 190 °C for 10 minutes in an oven. This process fuses the TPU and electrodes together, effectively integrating them. After heat treatment, the core shaft is removed, resulting in a hollow pump with internal spiral electrodes. It is crucial to note that the pump's architecture is intimately

linked to the diameter and count of TPU fibers, as well as the diameter of the core shaft. To fabricate fluid pumps with different internal diameters, adjustments in the quantity and inner diameter of TPU fibers are required to ensure that the spiral angle of the copper wires remains around 60°. In this study, the fluid pump specifications included an internal diameter of 1.4 mm, a length of 10~20 cm, a TPU fiber diameter of 0.4~0.6 mm with six strands, a copper wire diameter of 0.08 mm, and a CNT diameter of 20~50 μm. The driving fluid selected was hydrofluoroether Novec 7100 (3M).

The fluid-cooled artificial muscles are designed in both parallel and series configurations, with the heating mechanism for both structures provided by metal wires spirally wound around the nylon fibers.

In the parallel configuration of artificial muscles, the actuation component wraps around the exterior of the cooling section. Pre-twisted Nylon fibers (bias angle 34.3°), tightly coiled with 0.1 mm copper Cu wire, are meticulously wound around the outer surface of the fluid pump and then coiled around a core shaft to form a coil. This assembly is subjected to a heat treatment at 150 °C for 2 hours in an oven, followed by cooling to room temperature to produce an artificial muscle sheath on the cooling tube. It's important to note that TPU, under high temperatures, tends to soften or even melt, so care must be taken not to exceed appropriate heat treatment temperatures. Given TPU's inherent softness, the sample is prone to deformation during the winding process, potentially misaligning the spiral copper electrodes within the pump and altering its internal diameter. To prevent such deformation, a pillar made from high-melting-point materials (could be a nylon fiber) matching the pump's internal diameter is inserted into the pump during fabrication and removed it after thermal treatment. This step ensures the structural integrity and precise alignment of components within the fluid-cooled artificial muscle, critical for maintaining the system's operational efficiency and reliability.

For the series artificial muscle, the actuation and cooling sections are distinct. The actuation part is fashioned from hollow nylon fibers with different diameters (outside diameter 2~3 and an inner diameter of 1.5 mm). Under a load of 130~500 g, a significant twist is applied to the nylon tubes before mandrel coiling them around a core. The assembly is then heat-treated at 150 °C for 2 hours to relieve internal stresses induced by the twisting and winding processes and cooled to room temperature to finalize the coil structure of hollow artificial muscle. The final step involves connecting the fluid pump tube and the muscle at their respective lengths using a thermoplastic linking tube, thereby forming a series-configured FCAM.

FCAM conductive layer is a sandwich structure, consisting of conductive silica gel layer, high viscosity silica gel layer and nylon tube layer. The preparation process is as follows: mix the A glue and B glue of ordinary silica gel in a ratio of 1:1, and then add the conductive carbon black filler with different ratios to the above silica gel mixture, and use an overhead electric stirrer to stir vigorously for 30 min to form a homogeneous mixture. The C-type silicone tube was placed on the outside of the pre-twisted nylon tube as a mold for the conductive layer and the connecting layer, and then the high-viscosity silicone and the conductive silicone mixture was sequentially covered in the

inner test of the C-type mold, and placed in an oven for heat treatment at 100°C for 2 h. After curing and demolding, the fibers were wound around a mandrel to form an artificial muscle with a sensing layer.

2. The bias angle adjustment method

Adjusting the bias angle in the fabrication of artificial muscles is essential for optimizing their actuation characteristics. This meticulous process begins with securing a straight length of fiber material, such as nylon or nylon tube, between a fixed point and a motor's rotatable chuck. The objective is to achieve a precise bias angle (the angle between the fiber direction and the muscle's longitudinal axis), which significantly influences the muscle's contraction force, displacement, and overall work capacity.

To apply torsion, a weight (typically 500 g for the series muscle case), is suspended from one end of the fiber or tube, while the other end is attached to a motor. A tether on the weight prevents the fiber from rotating with the motor, ensuring that each rotation of the motor translates directly into a twist in the fiber or tube. The degree of torsion is carefully controlled to avoid exceeding the coil point of a specific fiber or tube, with a stepper motor employed to record the applied torsion and a camera to document the resultant bias angle on the tube surface (as shown in Figure S12).

This relationship between the bias angle and the number of twists is critical for determining the desired bias angle, following the equation below:

$$\alpha = \tan^{-1}\left(\frac{n\pi d}{L_1}\right) \quad (1)$$

Here, α is the angle formed between the helical structure of the twisted fiber and the longitudinal axis of the muscle, L_1 is the length of the fiber after twisting. The twisting process shortens the original length of the fiber (L_0) to L_1, n is the number of twists applied to the fiber, d is the diameter of the nylon fiber.

After achieving the target bias angle through precise torsion application, the twisted structure is fixed through heat treatment, to set the angle permanently and relieve any internal stresses. The final step involves assembling the artificial muscle by integrating the treated fiber with additional components like electrodes, depending on the specific design requirements.

3. Dual-mode heat dissipation mechanism for series FCAM

To elucidate the transient heat dissipation process during the cooling phase, the analysis was abstracted into a two-dimensional heat dissipation model, with an underlying assumption that temperature variations are predominantly radial. This premise is justified by the disproportionately high aspect ratio of the hollow tube, which dictates that radial thermal fluctuations significantly surpass axial changes. The tube is composed of a nylon polymer, characterized by its inefficacy as a thermal conduit.

The cooling dynamics of the hollow fiber artificial muscle encapsulate three distinct mechanisms: heat exchange between the external surface of the muscle tube and the ambient air, conductive heat transfer from the tube's outer to inner walls, and a

combination of forced convection and boiling heat transfer from the tube's inner surface to the circulating coolant. Each segment of this multifaceted cooling process is governed by specific control equations, reflecting the intricate interplay of thermal properties and fluid dynamics within this system.

The governing equation for the thermal conduction process spanning from the exterior to the interior wall of the hollow conduit is formalized as follows:

$$\rho_1 c_1 \frac{\partial T(r,t)}{\partial t} = \frac{k_1}{r}\frac{\partial}{\partial r}\left(r\frac{\partial T(r,t)}{\partial r}\right) \tag{2}$$

In the equation: ρ_1 represents the density of the hollow tube material, c_1 represents the specific heat capacity of the hollow tube material, k_1 is the thermal conductivity of the hollow tube material, T is the temperature of the tube wall at radius r and time t.

The governing equation for the convective heat transfer process between the outer wall of the hollow tube and the air is as follows:

$$q_{out} = h_{air} \bullet 2\pi r_1 \bullet (T(r_1,t) - T_3) \tag{3}$$

In the specified equation: q_{out} symbolizes the quantity of heat exchanged between the outer wall of the hollow tube and the surrounding air, h_{air} is the convective heat transfer coefficient characterizing the exchange from the air to the tube's external surface, r_1 indicates the external diameter of the hollow tube, T is the temperature of the tube wall at radius r_1 and time t, T_3 refers to the temperature of the surrounding environment.

The governing equation for the heat conduction process between the inner wall of the hollow tube and the cooling liquid is as follows:

$$q_{in} = h_{liq} \bullet 2\pi r_2 \bullet (T(r_2,t) - T_{liq}(x,t)) \tag{4}$$

In the specified equation: q_{in} represents the amount of heat transferred through convective heat exchange between the inner wall of the hollow tube and the cooling fluid, h_{liq} is the convective heat transfer coefficient from the cooling fluid to the inner wall of the tube, r_2 denotes the inner diameter of the hollow tube, T is the temperature of the tube wall at radius r_2 and time t, T_{liq} is the temperature of the cooling liquid at axial coordinate x and time t.

When the temperature of the cooling fluid approaches or exceeds its boiling point, boiling phenomena occur, introducing additional latent heat transfer. The control equation for this scenario is as follows:

$$q_{boil} = h_{boil} \bullet 2\pi r_2 \bullet (T(r_2,t) - T_4) \tag{5}$$

In the specified equation: q_{boil} represents the amount of heat transferred through boiling heat exchange between the inner wall of the hollow tube and the cooling fluid, h_{boil} is the boiling heat transfer coefficient for the cooling fluid, r_2 denotes the inner diameter of the hollow tube, T is the temperature of the tube wall at radius $r2$ and time t, T_4 is the boiling point of the cooling liquid.

The temperature of the cooling fluid T_{liq} (x, t), in relation to the fluid's initial temperature T_2, the fluid flow velocity v, and other factors. Thus, its temperature can be succinctly approximated through the following expression:

$$T_{liq}(x,t) = T_2 H(vt - x) \tag{6}$$

In the specified equation: T_{liq} is the instantaneous temperature of the cooling fluid at axial coordinate x and time t, T_2 represents the initial temperature of the cooling fluid, $H(.)$ denotes the Unit Step Function, v symbolizes the velocity at which the cooling fluid is flowing. The initial conditions are:

$$T(r_1, 0) = T_1 \tag{7}$$

4. Flow boiling heat transfer examination

As we describe in the main text and shown in Movie S2, in the experimental evaluation of series-configured muscles utilizing Hydrofluoroether (HFE) as a coolant, the heat absorption mechanism is emblematic of a flow boiling heat transfer phenomenon. This process intricately combines convective dynamics and boiling vaporization to expedite thermal energy transfer. As the fluid traverses the heating interface at a designated velocity, it absorbs externally applied thermal energy, instigating the vaporization of a fraction of the liquid into vapor within the flow continuum.

Several key advantages characterize the flow boiling heat transfer mechanism. Such as, the synergistic interaction between vapor and liquid in a biphasic flow substantially augments the thermal transfer efficiency. Bubble nucleation, growth, and detachment occur dynamically within the flow, facilitating rapid heat exchange across the gas-liquid interface. Continuous fluid movement mitigates the accumulation of vapor bubbles adjacent to the heating surface, significantly reducing the risk of localized superheating phenomena. Additionally, the perpetual flow ensures the consistent replenishment of unevaporated liquid at the heating interface, thereby optimizing the boiling heat transfer process for enhanced thermal efficiency.

The heat carried away by the evaporating fluid is denoted as:

$$Q_1 = m_1 \times L_v \tag{8}$$

The heat carried away by the heat exchange flow of the liquid is denoted as

$$Q_2 = m_2 \times c \times \Delta T \tag{9}$$

In the above equations, Q_1 represents the heat carried away by fluid evaporation, measured in joules, m_1 is the mass of the evaporating fluid in grams, and L_v signifies the latent heat of vaporization during the liquid-to-gas phase change, measured in joules per gram. Q_2 accounts for the heat removed by the convective motion of the fluid, also measured in joules, m_2 denotes the mass of the convective fluid in grams, c stands for the specific heat capacity of the fluid, with units, and ΔT represents the temperature change of the fluid in degrees Celsius.

Upon incorporating the empirically measured data into the prescribed formula, the

calculated heat dissipated via fluid evaporation is quantified at 145.996 J, while the thermal energy extracted through fluid motion amounts to 5.599 J.

5. Investigating influence of tube diameter on cooling effect

In accordance with the thermodynamic principles that govern our artificial muscles, the study also delved into how varying tube wall thicknesses influence muscle cooling capabilities. By maintaining a constant inner diameter and varying the wall thickness, we observed that thicker walls resulted in prolonged cooling and overall cycle times for both activated and non-activated pumps (as illustrated in Figure S15, A). The data indicate that muscles with thinner tube walls facilitate more efficient thermal exchange. Based on the data we absorbed, we utilize the thinnest wall thickness available in commercial nylon tubes for our experiments, aiming to optimize the cooling process.

6. Electrical power input versus muscle actuation dynamics

The study additionally examined the effect of varying electrical power inputs on the actuation performance of the muscles. It was found that increasing the input power led to a decrease in heating time (while cooling time remained unchanged), effectively shortening the overall cycle time. However, this adjustment also led to a gradual decrease in the tensile under identical load conditions. This phenomenon can be attributed to localized peak heating reaching up to 140 °C in a brief duration, which does not allow for efficient heat distribution throughout the material. Consequently, this results in a low thermal utilization efficiency and hampers the conversion of electrical energy into mechanical energy necessary for muscle contraction (as shown in Figure S15B, C).

7. Pump performance evaluation

For all tests, Novec 7100 from 3M was used as cooling fluid, following the method outlined in Figure S3. We measured the flow rate by collecting the volume of fluid passing through the pump within a set time using a graduated cylinder, determining the maximum flow rate at various voltages. Maximum pressure readings were taken when the pump's outlet was completely closed off, using a fluid pressure sensor from Shanyi (Shandong) Automation Instrument Co., Ltd, model SZY-101V20LC.

According to findings by Herbert Shea,[23] a linear pump reaches its peak efficiency and power density at half its maximum pressure and flow rate. The relationship between the pump's performance parameters is described by the equation:

$$\rho = \frac{\mathrm{Q_{max}}}{2} \times \frac{\mathrm{F_{max}}}{2} \tag{10}$$

$$\eta = \frac{\rho}{\mathrm{V_{input}} \times \mathrm{I_{input}}} \tag{11}$$

Where ρ stands for the pump's power density, Q_{max} is the maximum flow rate, F_{max} is the maximum pressure, η is the efficiency, V_{input} is the input voltage, and I_{input} is the input current.

8. The impact of increasing the number of carbon nanotubes (CNTs) on the performance of fluid pumps.

In our study, we enhanced the specific surface area of the fluid pump electrodes by helically winding CNT fibers around copper (Cu) wires, which significantly improved the efficiency of molecular ionization and, consequently, the fluid pump's performance. To further validate the impact of CNT fiber quantity on the performance of the fluid pump, we adjusted the spinning parameters of the CNT@Cu electrodes to achieve different winding pitches, ranging from 170 μm to 1024 μm. As shown in Figure S5, our analysis of the fluid pressure generated by the pump revealed that as the pitch of the CNT fibers decreased (resulting in a higher density of CNTs per unit length of the electrode), the pumping pressure at 5 kV increased from 1.1 kPa to 2.9 kPa. This result confirms that increasing the amount of CNT material can enhance the pumping capability of the fluid pump to a certain extent. While increasing the CNT winding density can indeed enhance the fluid pump's performance, we observed that higher winding densities also increase the bending stress on the CNTs during the winding process. Excessive winding density can cause CNTs to become disordered and break, leading to their detachment from the Cu wire and ultimately resulting in electrode damage

9. The working principle of the fluid pump

The working principle of the fluid pump is based on electrohydrodynamics (EHD), which drives fluid flow through the action of electric field forces on the charges within the fluid medium. Specifically, this process involves charge injection and field emission effects. When an external electric field is applied at a sufficiently high level, surpassing the tunneling threshold, electrons can overcome the energy barrier and tunnel directly from the cathode surface into the fluid medium. The fluid molecules that gain these electrons become negatively charged ions, which are then accelerated by the electric field toward the anode, where they discharge. During this process, the negatively charged ions drag the surrounding fluid molecules, inducing fluid flow. By using dielectric liquids with high electron affinity, such as hydrofluoroethers, it is possible to ensure that the energy barrier for field emission at the cathode is lower than at the anode, thereby generating a unidirectional net fluid flow under a DC electric field.

10. The sensing mechanism of composite sensing layers

We selected carbon black (CB)-doped silicone composite as the sensing layer material due to its effective piezoresistive properties. Incorporating CB into the insulating silicone matrix transforms it into a conductor when the CB content exceeds the percolation threshold, forming conductive pathways through particle contacts. When mechanical strain is applied to the sensing layer, the silicone matrix deforms, causing CB particles to separate along the direction of strain. This separation disrupts the conductive network, significantly increasing the electrical resistance, as illustrated in Fig. S16C. Upon releasing the strain, the matrix returns to its original shape, allowing CB particles to reconnect and restore the conductive pathways, thus reducing the resistance to its initial value. This reversible change in resistance due to mechanical

deformation enables the composite to function as an effective strain sensor, converting mechanical stimuli into electrical signals through the piezoresistive effect.

11. Sensing layer stability and responsiveness analysis

In the stability analysis of the sensing layer, we performed 2000 tensile unloading cycles on the artificial muscle sensing layer under the experimental conditions of tensile rate of 450 mm min-1 and tensile ratio of 50% and 500 tensile unloading cycles on the artificial muscle sensing layer under the experimental conditions of tensile rate of 150 mm min-1 and tensile ratio of 200%, respectively. From Fig. 4G and S19, it can be seen that the resistance-strain response characteristics of the sensing layer always remain stable. This stability is mainly caused by the fact that the composite material reaches a balance between the destruction and reconstruction of its internal conductive network after many tensile cycles, which results in the formation of a stable conductive pathway. Regarding the discussion of the responsivity of the sensing layer, we have performed the static and dynamic responsivity analyses, respectively. In the static responsivity analysis of the sensing layer, we respectively made rectangular standard specimens of conductive silica gel with different carbon black contents. The specimen is stretched to a specific tensile ratio using an electronic universal testing machine and then held at rest. A digital multimeter is then used to record the resistance of the specimen at that stretching ratio. As shown in Fig. S17A, with the increase of the proportion of carbon black in the conductive silica gel, the composite strain sensitivity showed first increasing and then decreasing. In addition, the sensitivity factor gauge factor (the instantaneous ratio of the relative change in electrical resistance to the tensile strain) was used to further evaluate the sensitivity of the sensing layer in response to strain. As shown in Fig. S17B, the conductive silica gel with 7% carbon black content possesses a wider strain range and higher strain sensitivity, which matches the frequency and stroke range of our muscle actuation. It can also be seen in Fig. S14E that the conductive layer can sensitively track the stroke changes of the artificial muscle. In the dynamic responsivity analysis of the sensing layer, after integrating the conductive silica gel with 7% carbon black content as the sensing layer onto the artificial muscle, the resistive strain response characteristics of the sensing layer were analyzed for different stretching speeds with the stretching ratio of the artificial muscle at 200%. It can be seen from Fig. S18 and Fig. 4E that the resistance of the sensing layer increased from 17 kΩ to 22 kΩ as the stretching rate increased from 50 mm min^{-1} to 200 mm min^{-1}. This phenomenon can be explained by the fact that an increase in the loading rate implies that the amount of stress change applied to the material per unit of time increases. As a result, the conductive network within the conductive silica gel matrix is more susceptible to damage, leading to an increase in the resistance change of the material. In addition, the composite material shows good signal stability at four different loading rates, which meets the requirements of strain-sensing materials for dynamic strain monitoring responsiveness.

12. Supplementary Figures (S1-S19)

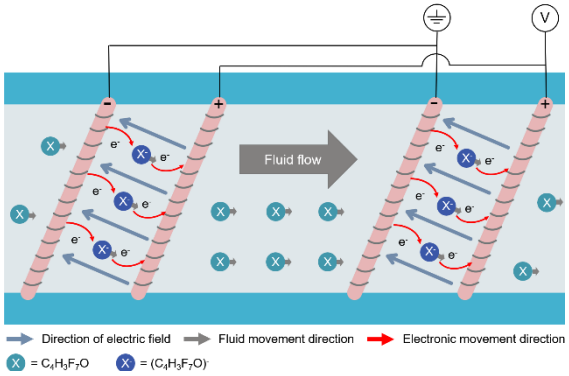

Figure S1. Fluid pump working mechanisms.

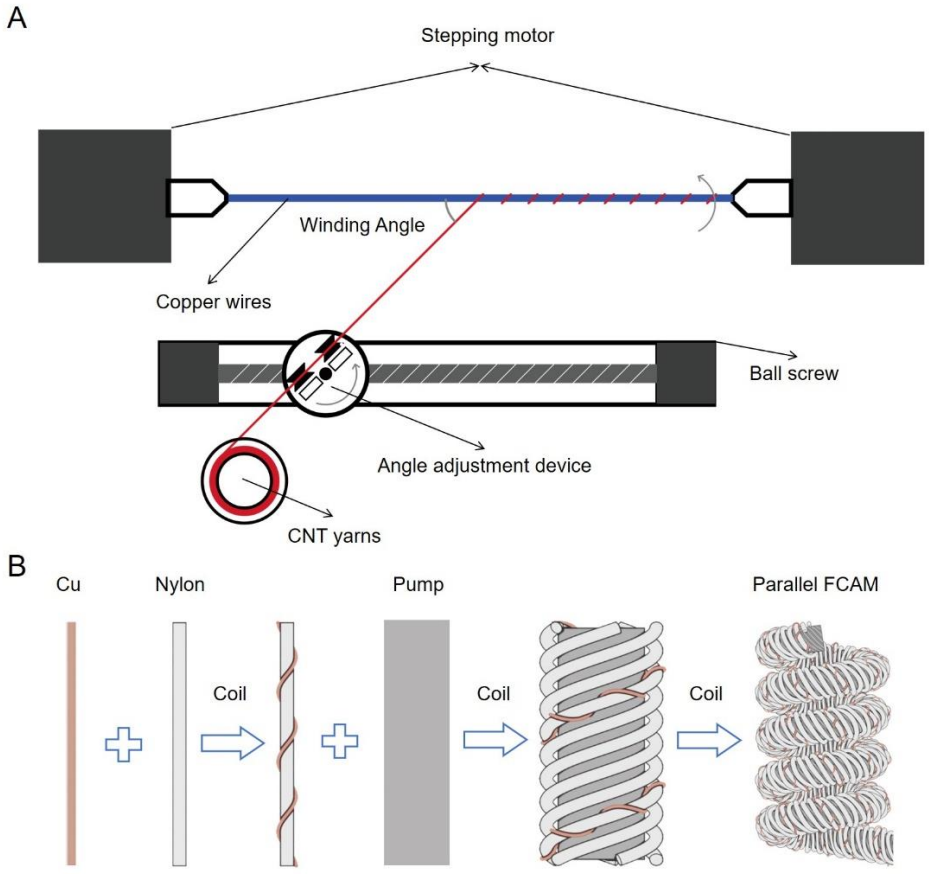

Figure S2. Schematic diagram of the process for preparing A) CNT@Cu electrodes and B) Parallel FCAM

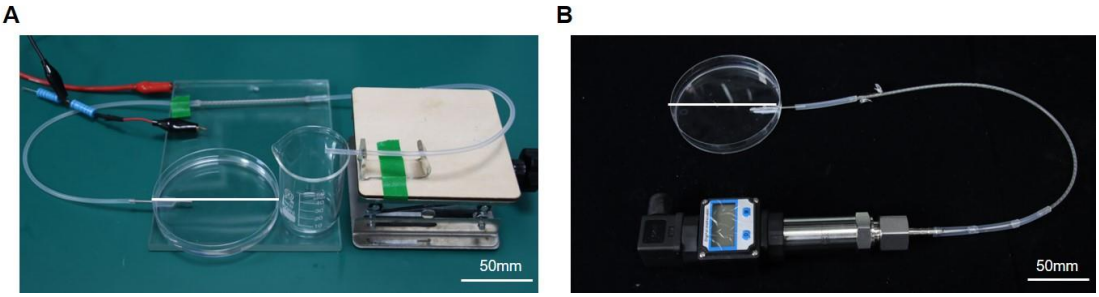

Figure S3. Methodology and setup for testing the flow rate A) and pressure B) of fluid cooling pumps.

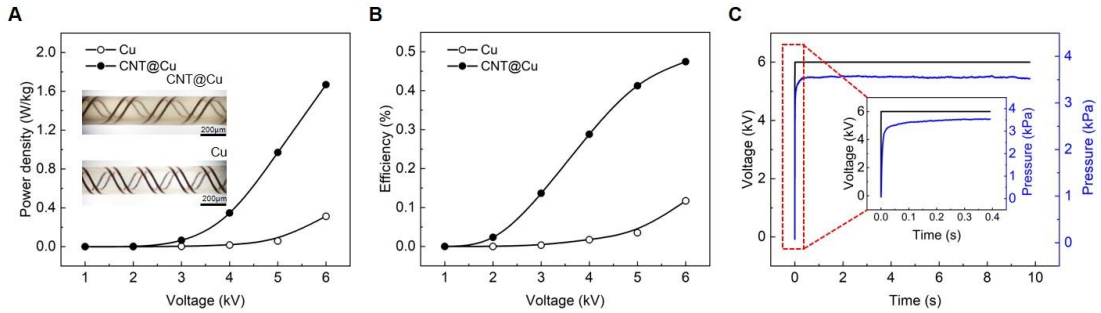

Figure S4. Performance metrics of pumps powered by Cu electrodes and CNT@Cu electrodes. A) Power density and B) Efficiency as functions of voltage variation. C) The relationship between voltage and fluid pressure over time during pump operation. The pressure-time curve at a constant driving voltage, showing the pump reaches its maximum stable pressure within 300 milliseconds and maintains steady output thereafter. All tests were conducted using a cooling pump with an inner diameter of 1.4 mm and a length of 100 mm.

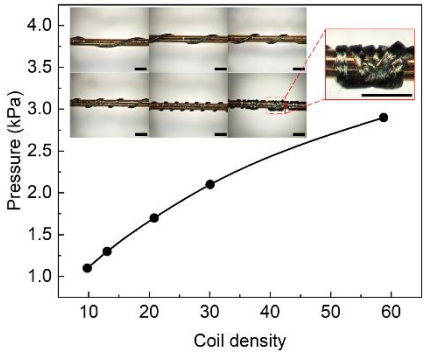

Figure S5. Fluid pump pumping pressure versus CNTs winding density of CNT@Cu electrodes. The driving voltage is 5 kV, the length of the fluid pump is 10 cm, the inner diameter is 1.4 mm, and the picture scale is 300 μm.

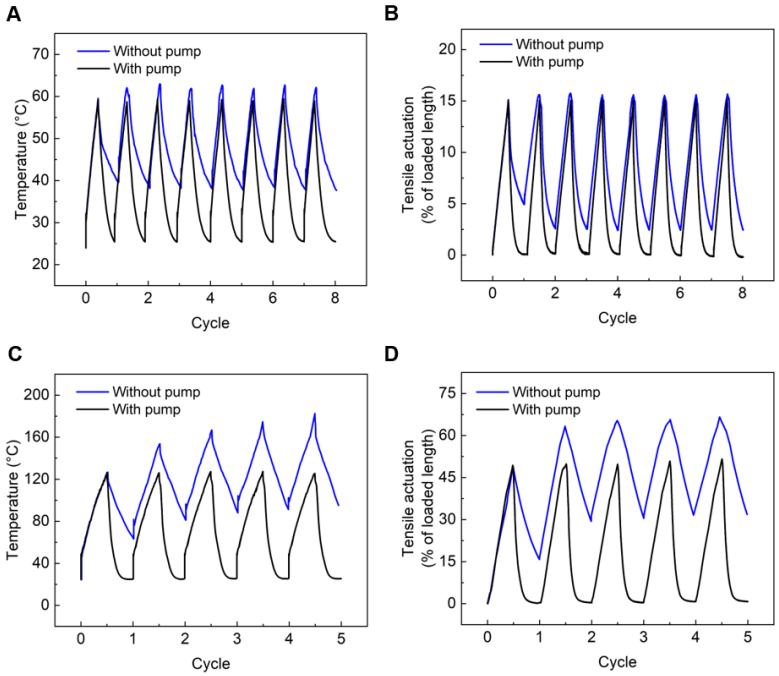

Figure S6. Temperature and tensile actuation curves over cycles for parallel and series FCAM with and without cooling pumps. A) The temperature and B) the tensile actuation variations over eight cycles for parallel FCAM, highlight the role of the pump in enabling the muscle to return to its initial state, thereby increasing the drive stroke. The spring index of the parallel FCAM is 4.5, with a muscle length of 200 mm (fully extended length) and a load of 15 kPa. C) The temperature and D) tensile actuation changes over five cycles for series FCAM with and without pumps, demonstrating the pump's effectiveness in restoring the muscle to its initial state and enhancing the tensile stroke. The series FCAM has a spring index of 3.7, a bias angle of 34.3°, a wall thickness of 0.75 mm, with a load of 0.18 MPa applying.

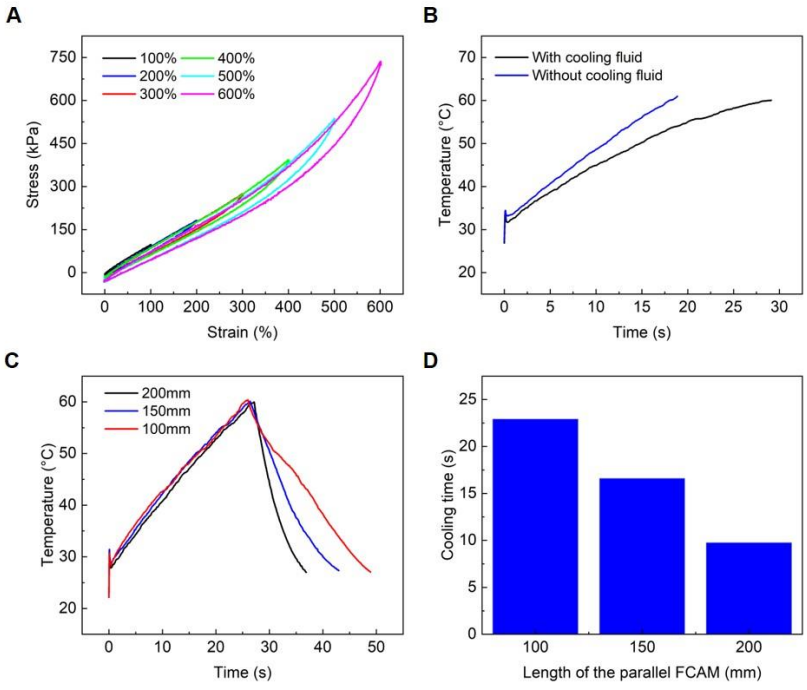

Figure S7. A) Mechanical performance testing of parallel FCAM. The spring index is 4.5 and this muscle is tested at a stretching speed of 30 mm min^{-1} B) Compares the rate of temperature rise in parallel FCAM muscles with and without internal coolant pre-filling. The spring index is 4.5, driven by a current of 2 A. C) Displays the temperature profiles over time for parallel FCAM of varying lengths, illustrating how length influences cooling behavior. D) Compares the cooling times for parallel FCAM with different lengths, demonstrating how muscle length affects pump cooling performance, associated with a muscle spring index of 4.5 and a drive current of 1.5 A.

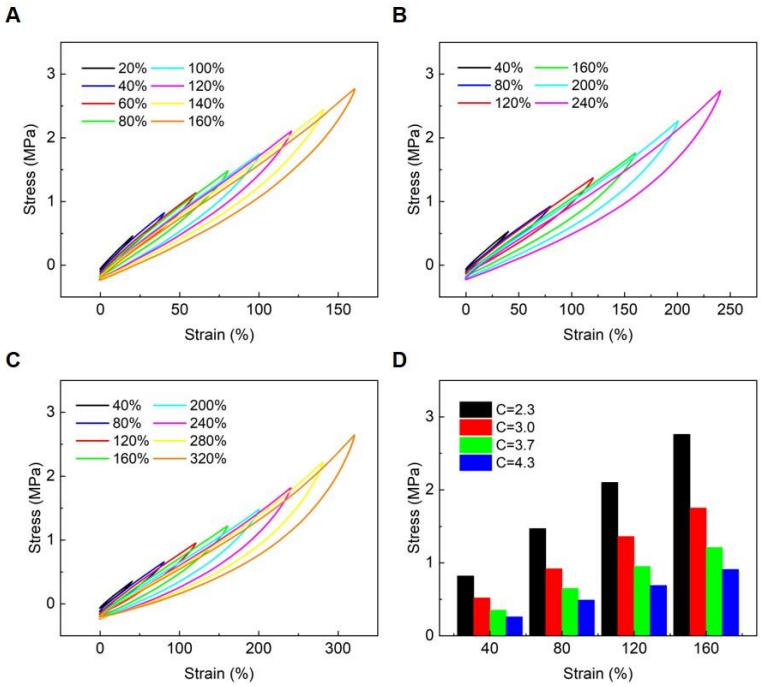

Figure S8. Mechanical performance testing of series FCAM with different spring indices under various tensile strains. A) The spring index is 2.3. B) The spring index is 3.0. C) The spring index is 3.7. D) Comparison of stress responses under the same strain for series FCAM with different spring indices. Each muscle has a twist angle of 34.3°, a wall thickness of 0.75 mm, and is tested at a stretching speed of 30 mm min^{-1}.

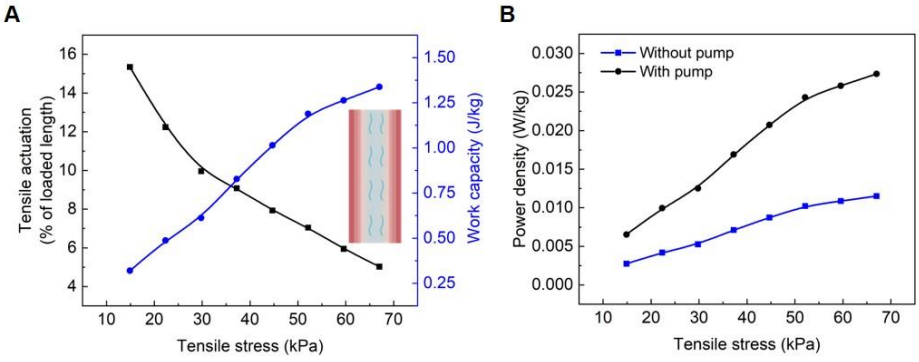

Figure S9. A) Tensile actuation and work capacity as a function of tensile stress for parallel FCAM. B) Power density variations under tensile stress for parallel fluid-cooled artificial muscles with and without pumps. These parallel FCAM samples had a spring index of 4.5, a driving current of 2 A, and a muscle length of 100 mm.

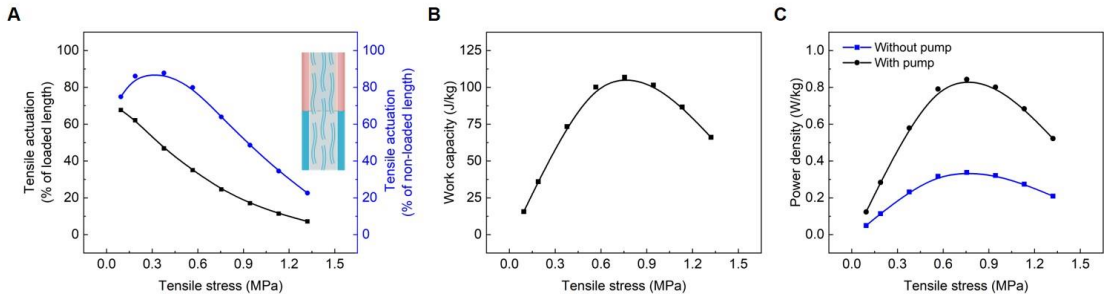

Figure S10. A) Tensile actuation for loaded and non-loaded lengths, and B) work capacity variation with tensile stress for series FCAM. C) Power density variations for series FCAM with and without pumps, under different tensile stress. The series FCAM employed a spring index of 4.3, a bias angle of 34.3°, a wall thickness of 0.75 mm, and an actuation temperature of 140 °C.

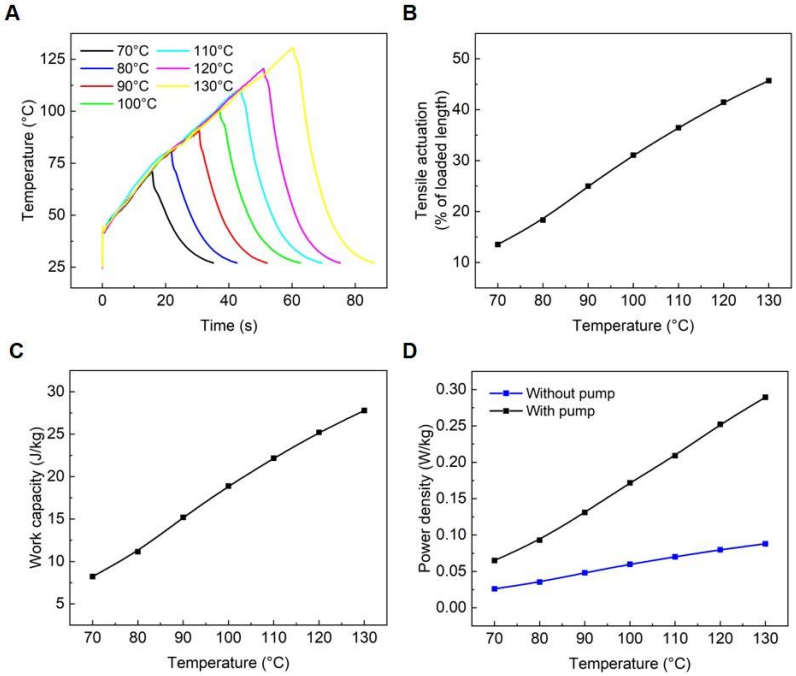

Figure S11. A) Temperature profiles over time for series FCAM at various actuation temperatures. B) Tensile actuation and C) work capacity curves across different actuation temperatures demonstrate the performance variability of series FCAM. D) Comparative power density at different actuation temperatures for series FCAM with and without pumps, highlighting the efficiency of the cooling system. The configurations utilized a spring index of 3.7, bias angle of 34.3°, and wall thickness of 0.75 mm with a 0.18 MPa load applied.

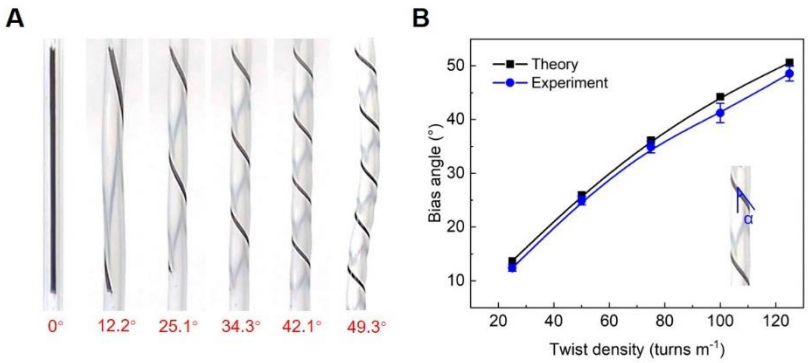

Figure S12. A) Images of nylon hollow tubes at different bias angles. B) Theoretical and experimental comparison of surface bias angle relationships with twist density on nylon tubes. The wall thickness is 0.75 mm, the twisting load is 0.94 MPa, and the twisting speed is 30 r/min.

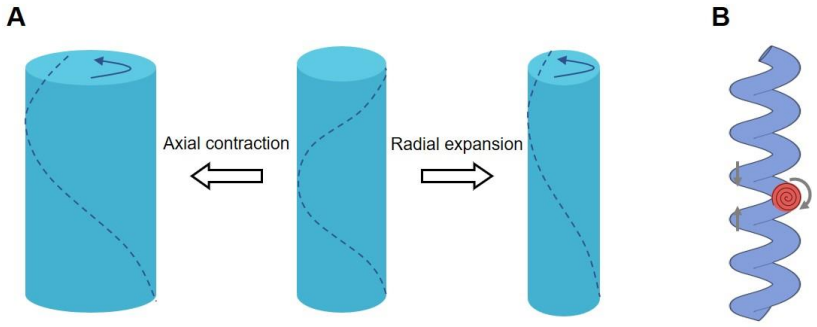

Figure S13. Illustration of volume expansion in twisted and helical artificial muscle fibers and its conversion into bias angle changes, facilitating contraction and expansion movements.

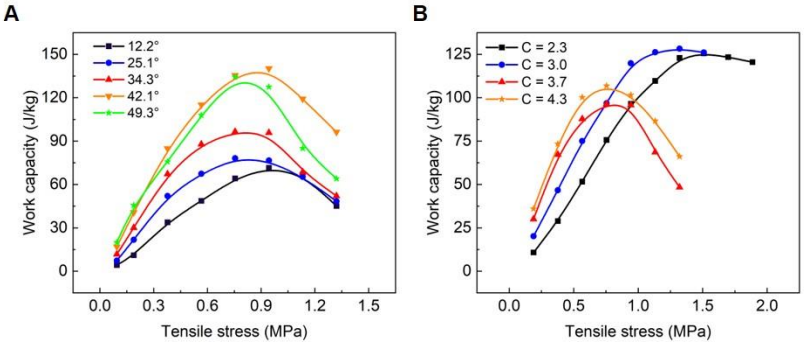

Figure S14. A) Work capacity variations with tensile stress for series FCAM at different bias angles. B) Work capacity variations with tensile stress for series FCAM at varying spring indices. The series FCAM with different spring indices have a bias angle of 34.3°, a wall thickness of 0.75 mm, and be actuated under 140 °C.

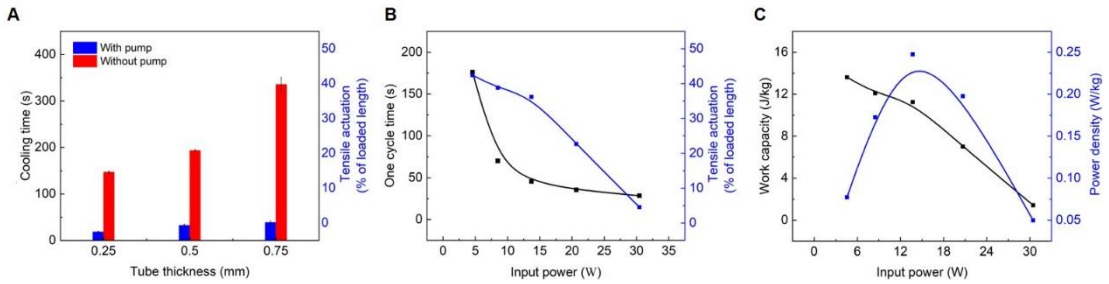

Figure S15. A) Cooling time comparisons for series FCAM with and without pumps under different wall thicknesses of Nylon tube. B) Cooling time and tensile actuation response performance with respect to input power for series FCAM. C) Work capacity and power density with respect to input power for series FCAM. The operational load was 0.18 MPa.

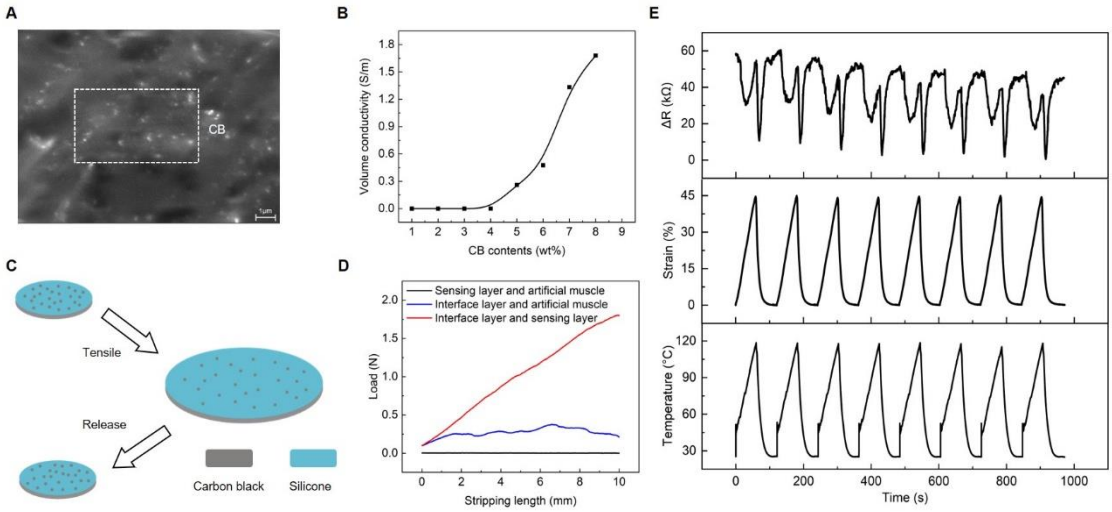

Figure S16. A) SEM microscopic morphology of conductive composites. Carbon black content is 7%. B) Volume conductivity of the composite material as a function of conductive particle filling ratio. C) Evolution of the conductive network during stretching processes, illustrating the mechanical-electrical property interplay. D) Comparison of mechanical peeling experiments across different interfaces. The sample width was 23 mm. Real-time monitoring of temperature, strain, and resistance during the operation of integrated drive-sensing muscles, emphasizing the sensor's responsiveness and stability.

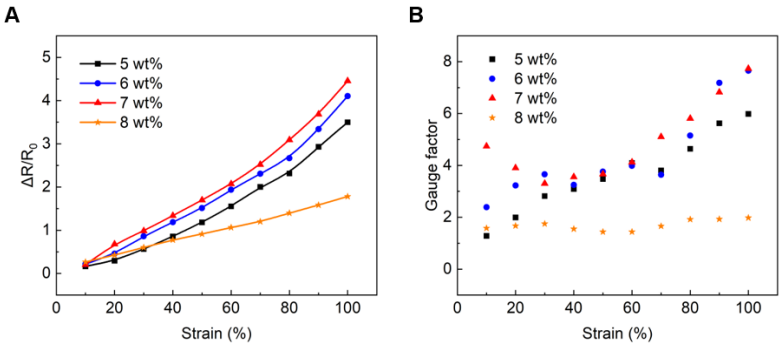

Figure S17. Curves of A) resistance and B) gauge factor of conductive silica gel sensing

layer with tensile strain for different carbon black contents.

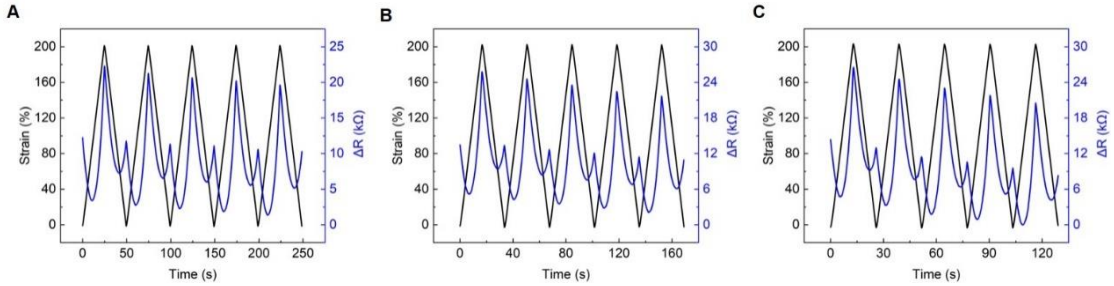

Figure S18. Resistance changes in the muscle sensing layer during multiple stretching cycles at different rates A) 100, B) 150, and C) 200 mm min^{-1}. The spring index, bias angle, and wall thickness of the muscle are 3.7, 34.3° and 0.75 mm respectively.

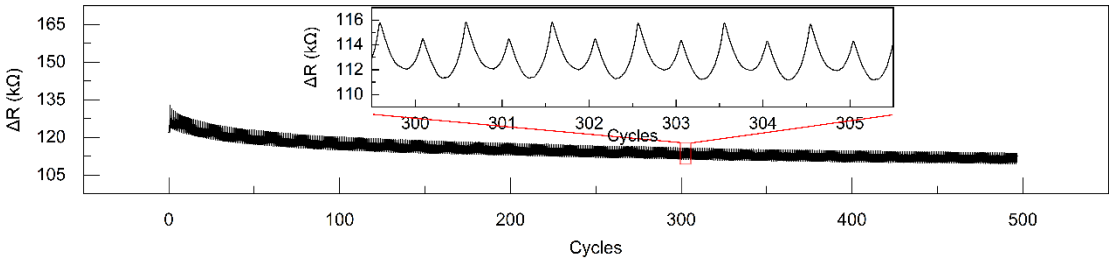

Figure S19. Resistance-strain response characteristics of the integrated artificial muscle over 500 cycles at a strain of 200% and a stretching rate of 150 mm min^{-1}.

13. Description of Supplementary videos

Movie S1.

Fluidic pump operation and performance testing of parallel and series FCAM.

Movie S2.

Flow boiling heat transfer demonstration.

Movie S3.

The actively anti-deflection artificial muscle composite material (with a load of 100 g).

Movie S4.

The actively anti-deflection artificial muscle composite material (non-load, pre bending).

Movie S5.

Integrating muscles as active driving units within mechanical assemblies (one unit).

Movie S6.

Integrating muscles as active driving units within mechanical assemblies (two units).

Movie S7.

Bio-inspired origami wrist joint movement demonstration